

ON THE MIXED SCATTERING MECHANISM ANALYSIS OF MODEL-BASED DECOMPOSITION FOR POLARIMETRIC SAR DATA

Wen Yang^{1, 2, *}, Hui Song¹, Gui-Song Xia², and Xin Xu¹

¹School of Electronic Information, Wuhan University, Luo-jia-shan, Wuchang, Wuhan 430072, China

²The State Key Laboratory of Information Engineering in Surveying, Mapping and Remote Sensing (LIESMARS), Wuhan University, 129 Luoyu Road, Wuhan 430079, China

Abstract—This paper introduces a simple but effective scattering mechanism identification scheme for analyzing mixed scattering mechanisms obtained by model-based decomposition. Using the normalized scattering vector, each pixel is represented by a point in a standard 2-simplex in \mathbf{R}^3 . Seven scattering category centers are represented by the three vertices, the three midpoints of sides and the centroid of the 2-simplex. The scattering category partitioning problem is then solved by minimizing the Euclidean distance between the image pixels and these category centers. The proposed scattering mechanism identification scheme is finally used for data analyzing and unsupervised classification. Experiments on AIRSAR and E-SAR L-band PolSAR images demonstrate the effectiveness of the proposed method.

1. INTRODUCTION

Polarimetric synthesis aperture radar (PolSAR) imagery has long been used as an appropriate and effective data source for many applications [1–3]. Unsupervised classification is a very important step in the processing of PolSAR data. In the past decades many classification methods have been proposed [4–12]. Some of these approaches use the inherent characteristic of PolSAR data and implement the classification with physical scattering mechanisms,

Received 6 April 2013, Accepted 22 June 2013, Scheduled 26 June 2013

* Corresponding author: Wen Yang (yangwen@whu.edu.cn).

see [4, 8, 9, 13–16]. One advantage of this kind of methods is providing information for scattering class identification [17, 18]. The polarimetric decomposition techniques used for scattering mechanism analysis can be roughly categorized into two groups:

- Methods based on the Cloude-Pottier target decomposition theory [19]. Denote H as the entropy, α as the average alpha angle and A as the anisotropy. In order to identify the scattering mechanisms, Cloude and Pottier [13] proposed to partition the H - α plane into eight zones, and further refine the results by utilizing the anisotropy A [15]. Ferro-Famil et al. [8] also presented a canonical scheme for the identification of scattering mechanisms by segmenting the “ H - A ” plane.
- Model-based decomposition, e.g., the three-component decomposition (also known as Freeman decomposition) [20]. Using the Freeman decomposition, Lee et al. [9] proposed a classification method for preserving scattering characteristics, which divides pixels into three basic scattering categories, i.e., surface, volume and double bounce scattering. To further analyze the mixture areas where scattering mechanisms exist, Yang et al. [21] used a more precise scheme to partition the scattering category by introducing the scattering power entropy and anisotropy.

In the classification algorithms mentioned above, scattering mechanism identification plays an important role. Although Cloude’s eigenvalue-based decomposition always yields a unique solution mathematically, how to interpret the results in terms of known scattering mechanisms is not clear yet [22, 23]. The model-based decompositions attempt to fit the PolSAR data with a three-component [20, 24–27] or four-component [28–30] scattering mechanism model, which has physical meanings, and usually lead to straightforward representations.

In [9], the scattering mechanism identification is achieved by using the dominance of the backscattering power obtained by Freeman decomposition. It is worth noticing that there are actually a large number of pixels whose dominant scattering mechanisms are not clearly defined, and further analysis of these pixels with hybrid scattering mechanisms is necessary. Lee et al. [9] extended the scheme by dividing these pixels into a mixed scattering category with predefined threshold. However, more detailed scattering mechanism identification is desirable. Considering all the possible combinations of the scattering mechanisms, and inspired by the work of Cloude and Pottier [13], Yang et al. [21] presented a seven-scattering-category scheme by partitioning the plane of the scattering power entropy and the anisotropy. Zhang et al. [31] addressed this problem by combining

the model-based decomposition and the rule-based segmentation for estimating the relative strength. The schemes in [21, 31] are elaborate, but their performances depended on some ad-hoc thresholds which are empirically selected. This paper attempts to solve the scattering mechanism identification problem in a more direct way.

We propose a simple but effective scheme for scattering mechanism identification. The vectors of the scattering powers obtained by the three-component decompositions are first normalized. Since elements for each normalized scattering vector are summed to one, pixels are represented by points in the standard 2-simplex in \mathbf{R}^3 . Vertices of the standard 2-simplex can be interpreted as pure scattering category centers. The scattering mechanism identification is thus achieved by classifying points on the standard 2-simplex via minimizing the Euclidean distance. The decision boundaries can be easily determined and no threshold is needed. This scheme also provides a visualization approach for analyzing the scattering characteristics of the three-component decomposition in different scenes. We test the proposed scheme on the classic Freeman-Durden decomposition [20], and the newly proposed adaptive model-based decomposition [26]. Experiments on data analysis and unsupervised classification with AIRSAR and E-SAR L-band PolSAR images demonstrate the effectiveness of the proposed method.

The rest of paper is organized as follows: Section 2 first presents the proposed scheme for the scattering mechanism identification, Section 3 then shows and analyzes the experimental results. In Section 4 the extensions and limitations of the proposed method are discussed, and finally conclusions are made in Section 5.

2. SCATTERING MECHANISM IDENTIFICATION

2.1. Model-based Three-component Decomposition

There are many polarimetric decomposition methods for scattering mechanism analysis, among which those “model-based” decompositions [22] of the covariance matrix or the coherency matrix attract much attentions, as they provide better physical understanding for the results. The Freeman decomposition (shorten as FMD) is a widely used model-based decomposition for its simplicity and stability. This decomposition expresses the measured covariance matrix as the sum of three physical scattering components: the surface, volume and double-bounce components.

$$\langle [C] \rangle = f_v \langle [C_{vol}] \rangle + f_d \langle [C_{double}] \rangle + f_s \langle [C_{surface}] \rangle. \quad (1)$$

The contribution of each scattering mechanism can be estimated according to the span

$$Span = |S_{HH}|^2 + 2|S_{HV}|^2 + |S_{VV}|^2 = P_S + P_V + P_D. \quad (2)$$

where P_S , P_V and P_D correspond to the power contributions of each scattering mechanism respectively.

Freeman decomposition assumes reflection symmetric for measure covariance and may result in many pixels with negative powers. The nonnegative eigenvalue decomposition (NNED) model [25] can avoid negative powers and is further extended to adaptive model-based decomposition (shorten as AMD) [26] by using a general volume component [32]. The covariance matrix can be written as

$$\langle [C] \rangle = f_v \langle [C_{vol}(\theta_0, \sigma)] \rangle + f_d [C_{double}] + f_s [C_{surface}] + [C_{remainder}]. \quad (3)$$

The general volume term $\langle [C_{vol}(\theta_0, \sigma)] \rangle$ is parameterized by the mean orientation angle θ_0 and the degree of randomness σ . The last term $[C_{remainder}]$ may include additional cross-polarized power that can represent terrain effects and rough surface scattering. It also can be used for determining the best fit parameters.

2.2. Scattering Mechanism Identification

In Lee's preserving scattering characteristic classification algorithm [9], pixels were divided into three basic canonical scattering categories by the dominance in backscattering power of P_S , P_V and P_D for surface ("Odd"), volume ("Vol") and double-bounce ("Dbl") scattering. Considering the situations in which many pixels have two or three nearly equal scattering powers and the dominant scattering mechanism is not clearly defined, Lee defined an additional "mixed" category by

$$\frac{\max(P_S, P_V, P_D)}{P_S + P_V + P_D} \leq C_t. \quad (4)$$

C_t is a predetermined parameter, normally between 0.4 ~ 0.8. However, it is still difficult to distinguish different mixed scattering mechanisms, since there exist four different types: "Odd + Vol", "Odd + Dbl", "Vol + Dbl" and "Odd + Vol + Dbl".

In this work, we developed a simple but effective scattering mechanism identification scheme for model based decomposition. We first define a three-dimensional normalized vector \mathbf{p} for each pixel

$$\mathbf{p} = [p_s, p_v, p_d]. \quad (5)$$

where p_s , p_v and p_d are normalized by their total scattering contribution, and represent the relative magnitude of the three power values P_S , P_V and P_D . We call \mathbf{p} the normalized scattering vector.

In this case, each pixel is on the standard 2-simplex in \mathbf{R}^3 due to $p_s + p_v + p_d = 1$. The standard 2-simplex in \mathbf{R}^3 is defined as

$$p_s + p_v + p_d = 1, \quad p_s \geq 0, \quad p_v \geq 0, \quad p_d \geq 0. \quad (6)$$

The standard 2-simplex in \mathbf{R}^3 is shown in Fig. 1(a). The coordinates of the three vertices A , B and C are $(1, 0, 0)$, $(0, 1, 0)$ and $(0, 0, 1)$, respectively. Each of the three vertices represents a pure basic scattering mechanism. If a pixel is very close to one of the vertices, then it shows dominant scattering mechanism associated to that vertex, otherwise, its dominant scattering mechanism cannot be clearly defined. Therefore we can call these vertices the “scattering category center points” (SCCPs). By this means, the three basic scattering categories partition scheme of Lee et al. [9] can be regarded as a minimum euclidean distance classification in the standard 2-simplex. For the case of Lee’s four categories scheme, it is equivalent to add a fourth category, whose SCCP is $D(1/3, 1/3, 1/3)$. This SCCP is the centroid of the 2-simplex which means that the contributions of the three canonical scattering are equal. The boundary of mixed category is determined by the threshold C_t . When we increase C_t , the area of the mixed category in the 2-simplex will increase too, which means more pixels may be classified into this category. The decision boundary is shown in Fig. 1(b) for $C_t = 0.5$.

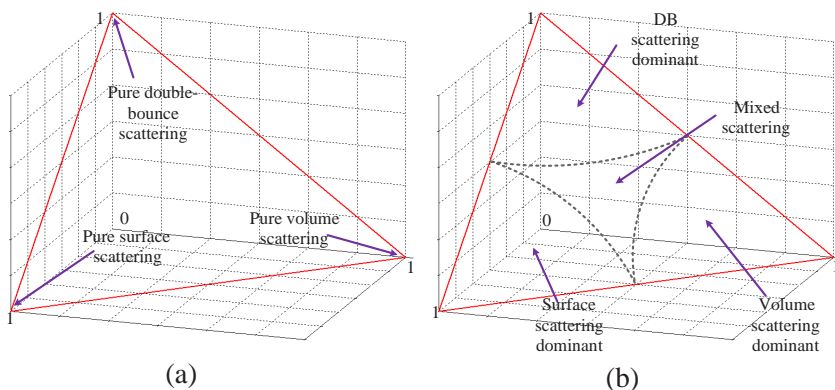


Figure 1. Mapping the scattering mechanisms of pixels into points in a 2-simplex plane. (a) The 2-simplex in \mathbf{R}^3 . (b) The decision boundaries for four scattering categories when C_t is 0.5.

To illustrate the type of mixed scattering mechanisms, we select an region from AIRSAR L-band PolSAR image over San Francisco. The normalized scattering vectors were calculated after applying FMD.

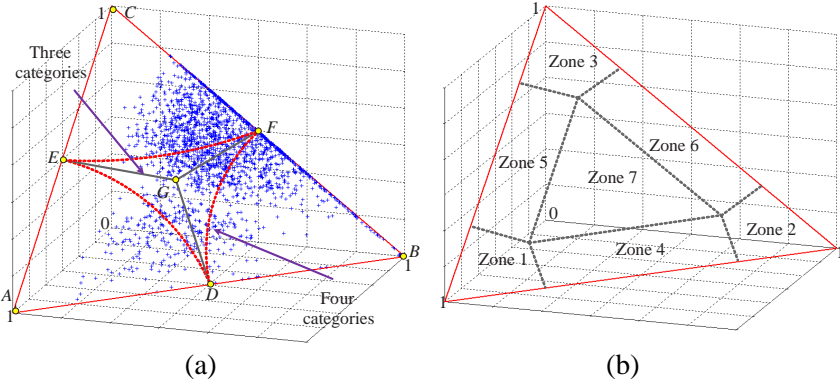


Figure 2. (a) Scatter diagram of selected areas (as marked in Fig. 3(b)) on standard 2-simplex. (b) Decision boundaries of proposed seven scattering categories identification scheme.

Scatter diagram of the normalized scattering vectors in standard 2-simplex is shown in Fig. 2(a). The solid dark lines are the boundaries for three categories and the red dashed lines are the boundaries for four categories. From Fig. 2(a), we can find that there are many pixels appear in the center area of the 2-simplex, whose dominant scattering mechanism cannot be clearly defined. This can be obviously mitigated when we add a mixed scattering category.

Inspired by the analyzing of the relative relationship between the three eigenvalue of Cloude decomposition, Yang et al. [21] considered a seven scattering categories partition scheme by introducing scattering power entropy H_p and A_p anisotropy for the Freeman decomposition.

$$H_p = - \sum_{i=1}^3 P_i \log_3 P_i, \quad A_p = \frac{b - c}{b + c}. \quad (7)$$

and

$$P_1 = \frac{P_S}{P_S + P_V + P_D}, \quad P_2 = \frac{P_D}{P_D + P_S + P_V}, \quad P_3 = \frac{P_V}{P_S + P_V + P_D}. \quad (8)$$

where $\langle a, b, c \rangle = \text{sort}(P_S, P_V, P_D)$, sort is an ordering function, and a, b, c is the ranking result from the biggest to the smallest. In terms of H_p and A_p , all pixels can be divided into seven categories, which are shown in Table 1, and more details can be found in [21]. then pixels with mixed mechanism are divided into four categories: “Odd + Vol”, “Odd + Dbl”, “Vol + Dbl” and “Odd + Vol + Dbl”. However, the entropy and anisotropy may be ambiguous for measuring the relative

relationship of the scattering power, the decision boundaries of the H_p and A_p plane should be determined very carefully.

In fact, the four mixed categories can be easily determined in the standard 2-simplex. For example, the fourth category “Odd + Vol” means that the two scattering mechanisms: surface and volume are dominant, moreover P_S and P_V are very close. The extreme case is that $P_S = P_V = 0.5 \times Span$, which corresponds to the center point $D(0.5, 0.5, 0)$ of the side between $A(1, 0, 0)$ and $B(0, 1, 0)$ in the 2-simplex. Similarly, the “Odd + Dbl” category corresponds to the point $E(0.5, 0, 0.5)$ and the “Vol + Dbl” category corresponds to the point $F(0, 0.5, 0.5)$, the last category “Odd + Vol + Dbl” corresponds to the centroid point $G(1/3, 1/3, 1/3)$ of the 2-simplex. Thus the points $A \sim G$ are the SCCPs for the seven categories scheme. The decision boundary can be determined by calculating the euclidean distance between the image pixels and these SCCPs, as shown in Fig. 2(b).

Table 1. Seven scattering categories with H_p and A_p .

	Low H_p , arbitrary A_p	High H_p , high A_p	High H_p , low A_p
Main scattering mechanism	Odd	Vol + Odd	Odd + Vol + Dbl
	Dbl	Odd + Vol	
	Vol	Odd + Dbl	

Table 2. Seven scattering categories and their SCCPs.

zone 1	Surface scattering dominant area. (“Odd”.)	$A(1, 0, 0)$
zone 2	Volume/canopy scattering dominant area. (“Vol”.)	$B(0, 1, 0)$
zone 3	Double-bounce scattering dominant area. (“Dbl”.)	$C(0, 0, 1)$
zone 4	Surface and volume hybrid scattering area. (“Odd + Vol”)	$D(0.5, 0.5, 0)$
zone 5	Surface and double-bounce hybrid scattering area. (“Odd + Dbl”)	$E(0.5, 0, 0.5)$
zone 6	Volume and double-bounce hybrid scattering area. (“Vol + Dbl”)	$F(0, 0.5, 0.5)$
zone 7	Triple hybrid scattering area. (“Odd + Vol + Dbl”.)	$G(1/3, 1/3, 1/3)$

The seven zones with different scattering mechanisms and their SCCPs are summarized in Table 2.

The zones 1 ~ 3 represent the three basic canonical scattering mechanisms, and others represent mixed scattering mechanisms. By using the normalized scattering vector \mathbf{p} , each pixel is represented by a point on a standard 2-simplex in \mathbf{R}^3 . The mathematical and physical meaning of this expression is very intuitive. It also provides visualization for analyzing scattering mechanism of the three-component decomposition. By rendering the scatter diagram in the 2-simplex, the distribution of the scattering mechanism can be observed directly when the points appear in different zones.

3. EXPERIMENTAL RESULTS

In this section, we investigated the performance of the proposed scattering mechanism identification scheme on real PolSAR data. NASA/JPL L-band AIRSAR data of San Francisco was used in our experiments. The image has 1024×900 pixels and the spatial resolution is about $10 \text{ m} \times 10 \text{ m}$. Speckle filtering (5×5 Boxcar filter) was applied to obtain sufficient averaging. The corresponding optical image was shown in Fig. 3. The two typical three-component model-based decompositions: FMD and AMD were used for testing. Figs. 4(a) and (b) show the polarization pseudo-color synthesized images of the two decompositions with $|P_S|$, $|P_V|$ and $|P_D|$ for blue, green and red.

3.1. Data Analyzing and Visualization

To further analyze the mixed scattering mechanisms, six sample regions marked in Fig. 3 are selected, each sample region has 20×20 pixels.

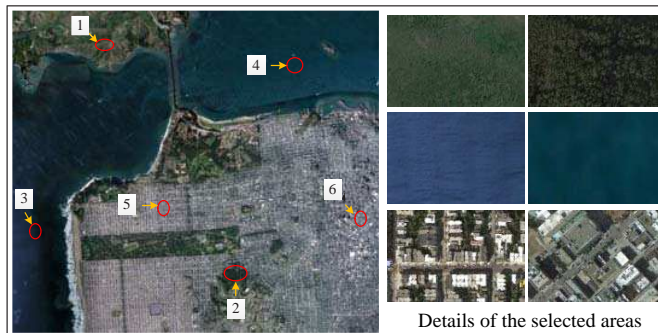


Figure 3. The corresponding optical image of San Francisco data from Google earth©.

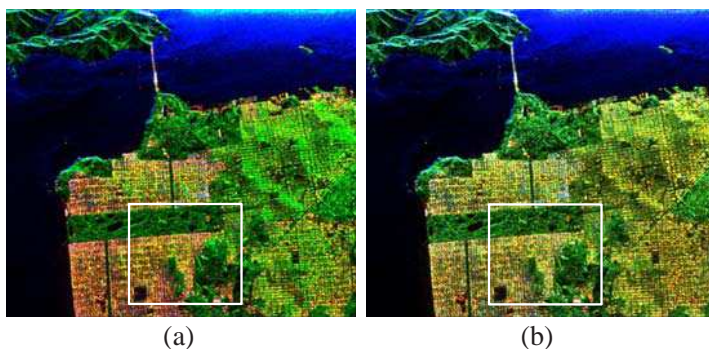


Figure 4. NASA/JPL AIRSAR PolSAR image of San Francisco. (a) FMD polarization pseudo-color synthesized image. (b) AMD polarization pseudo-color synthesized image. ($|P_S|$ -blue, $|P_V|$ -green and $|P_D|$ -red).

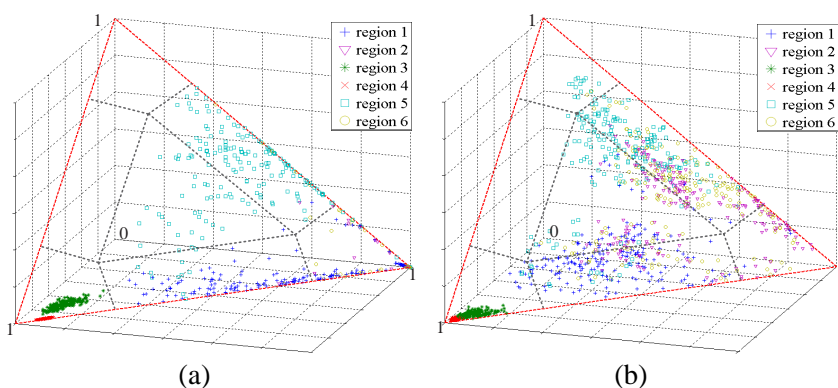


Figure 5. Scatter diagram of the normalized scattering vectors on 2-simplex plane. (a) Scatter diagram of FMD. (b) Scatter diagram of AMD.

These sample regions consist of three different land covers. Region 1 and 2 are vegetation areas, region 3 and 4 are ocean surface, region 5 and 6 contain different built-up areas. After applying model-based decompositions, the normalized scattering \mathbf{p} is calculated for each pixel. Then, each pixel is represented by a point on 2-simplex. The scatter diagrams of the sample regions using FMD and AMD are shown in Figs. 5(a) and (b), respectively.

From Fig. 5 we can see the scattering behaviors of the sample regions under different decomposition directly. For example, region 1 and 2 are both vegetation areas, but one comes from forest in

mountain areas and the other comes from dense trees in the urban area. For FMD, the pixels in region 1 cover zone 2 (“Vol”) and zone 4 (“Odd + Vol”), while pixels in region 2 mainly fall in the volume scattering dominant zone. The pixels in these two regions under AMD show more complex scattering mechanisms. The pixels in region 1 cover zone 4 (“Odd + Vol”), and the pixels in region 2 cover all volume related zones. The two ocean surface regions are consistent for the two decompositions: all pixels fall into a small region in zone 1 (“Odd”). As we know the urban areas are one of the most complicated terrain types, which are composed of various natural and artificial objects. For FMD, the pixels of region 5 fall into the volume and double-bounce scattering hybrid area-zone 6 (“Vol + Dbl”) and zone 7 (“Odd + Vol + Dbl”), the triple hybrid area. However, the pixels of region 6 all fall into the volume dominant zone 2 (“Vol”). For AMD, some of the pixels coming from region 5 fall into zone 3 (“Dbl”), showing double-bounce dominant scattering mechanism. The pixels of region 6 cover 4 different hybrid scattering zones. The differences showed by pixels in region 5 and 6 due to the fact that the buildings of region 5 and region 6 have different orientations. In addition, more pixels in the volume scattering dominant areas using AMD show hybrid scattering mechanism.

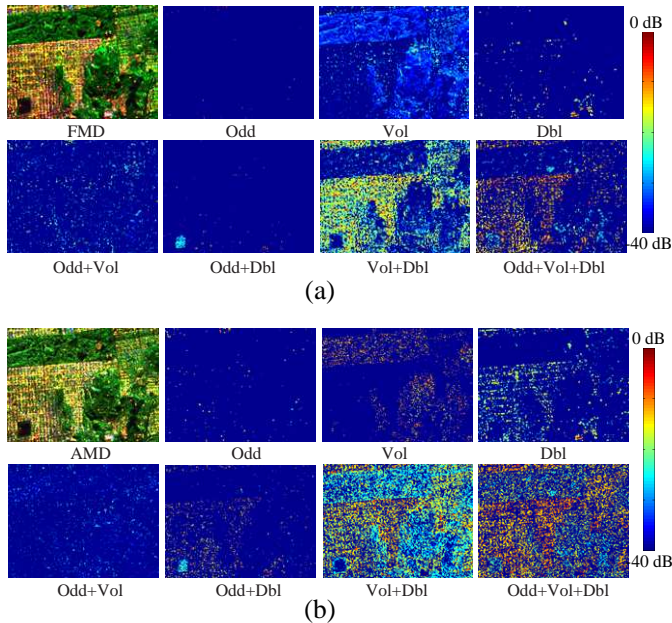


Figure 6. The powers of pixels in different scattering categories for the selected areas. (a) The results under FMD and (b) the results under AMD.

A bigger area marked in Figs. 4(a) and (b) is selected to demonstrate the complex scattering mechanisms contained in natural scenes. Figs. 6(a)~(b) show the results using FMD and AMD respectively. We show the pixels belonging to each scattering category by their power values. The power values are normalized by the maximum of each category in dB. These images reveal the scattering types and the ranges of the scattering powers. For FMD, the forest areas mainly show volume scattering dominant mechanisms, these pixels show very close scattering powers. There are also several strong scatters, whose powers are very high. The urban areas mainly consist of pixels with volume and double-bounce hybrid scattering (“Vol + DbI”) and the triple hybrid scattering (“Odd + Vol + DbI”). For AMD, we can find the pixels in volume scattering dominant category have higher powers than FMD, because the AMD with general volume term obtains a better fitting to the measurements. In the forest areas, unlike the case in FMD, many pixels show volume hybrid scattering (“Vol + DbI” and “Odd + Vol + DbI”). In the urban area, there are more pixels showing double-bounce scattering. The two decompositions achieve consistent result for describing the sports ground in the left bottom, this area show surface and double bounce scattering (“Odd + DbI”).

As we can see, for complicated natural scenes, the proposed seven scattering categories identification scheme provides a discriminative approach for analyzing hybrid scattering mechanism.

3.2. Classification

To further illustrate the effectiveness of the proposed scheme, we consider incorporating our scattering mechanism identification scheme with unsupervised classification. The seven basic categories partitioning scheme can be used as the initial segmentation. We use a similar classification scheme that proposed in [21] for illustration. Here we introduced the algorithm briefly.

- (1) Apply three-component model-based decomposition for each pixel, and compute scattering powers, P_S , P_D and P_V . After that the normalized scattering vectors are calculated.
- (2) Divide all pixels into seven categories as defined in Section 2. The euclidean distances between pixels and the seven SCCPs are calculated and the pixels are assigned to the categories with the minimum distance.
- (3) Dividing the pixels of each category into 15 clusters, then we have a total of 105 initial clusters. Within each category, the initial clusters are merged to a given desirable number of classes N_d based on the between-cluster Wishart distance [9]. We determine the

final number of classes in the i th category simply by its proportion to the total pixels.

- (4) Iteratively apply the Wishart classifier for three to five times to refine the results.

3.2.1. Results of AIRSAR San Francisco Data

The initial seven categories segmentations corresponding to the two decompositions are shown in Figs. 7(a)~(b). From these images, we can find the seven scattering categories identification scheme revealed rich contents of the scene. For the traditional FMD, the volume scattering contributions may be overestimated, therefore the pixels in the vegetation areas and the right urban areas in Fig. 7(a) are almost all classified into the second scattering category, which is volume scattering dominant. While in Fig. 7(b), the vegetation areas show hybrid scattering mechanisms, some pixels are assigned to the fourth category (“Odd + Vol”) and some are assigned to the sixth category (“Vol + Dbt”). Unlike the FMD that few pixels are assigned to the seventh category (“Odd + Vol + Dbt”), many pixels in urban areas

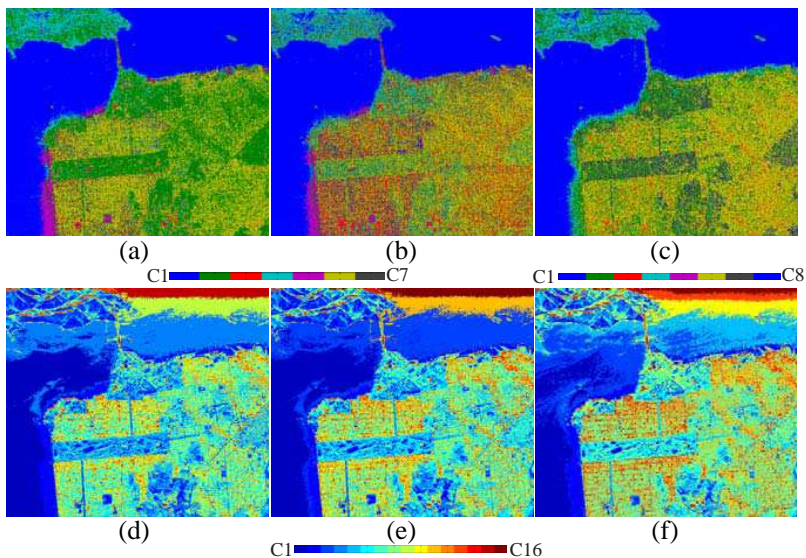


Figure 7. Classification results on AIRSAR San Francisco data. (a) Seven classes initial segmentation using FMD. (b) Seven classes initial segmentation using AMD. (c) The initial segmentation using H-alpha decomposition. (d)~(f) Final classification results after iterated clustering corresponding to (a)~(c).

show triple hybrid scattering mechanisms for AMD. The same case appears for the third category (“Dbl”), there are more pixels in urban areas show double-bounce scattering dominant For AMD.

After the initial seven scattering categories segmentation, pixels in each category were divided into many small clusters and then were merged to a given desirable number of classes. The total number of classes was 16. When merging was completed, the iterated Wishart classifier was applied for refinement. The final classification results for the three decompositions are shown in Figs. 7(d)~(e). For better comparison, we rearranged the labels by the average powers of each classes from low to high. We use cold colors for classes with low average powers and warm colors for classes with high powers. For the two model-based decompositions, the final results both show good performance. The details of the ocean surface are well distinguished. The street patterns associated with city blocks are clear and the vegetation areas show rich texture information.

We also compared the results with the $H/A/\alpha$ -Wishart classification algorithm, which finally segments the image into 16 classes. Fig. 7(c) shows the 8-classes segmentation map by partitioning the H - α plane. Though the $H/A/\alpha$ decomposition is roll-invariant, the buildings around region 6 which do not aligned in the along track direction are still misclassified as forest areas.

3.2.2. Results of DLR E-SAR Data

The experimental L-band PolSAR data was collected by DLR E-SAR system from the Oberpfaffenhofen area of Germany. The image size

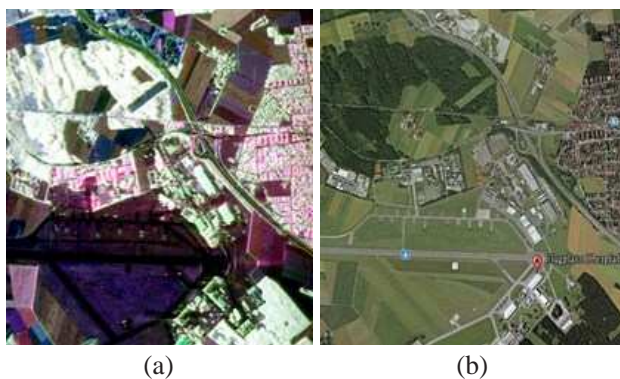


Figure 8. E-SAR PolSAR data set over Oberpfaffenhofen. (a) Colored image with Pauli matrix components. (b) The corresponding optical image from Google earth©.

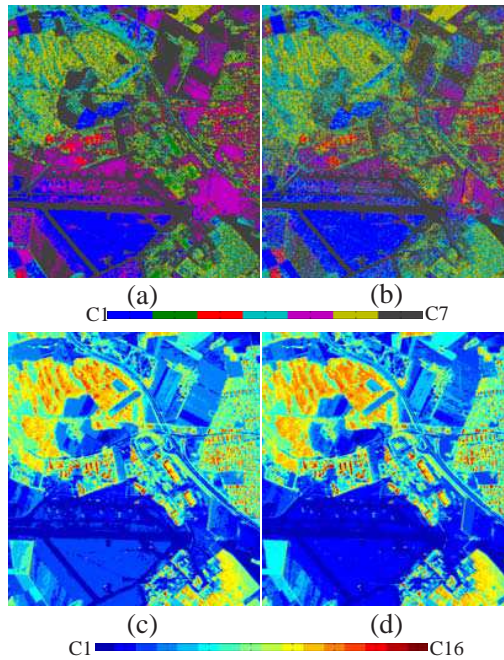


Figure 9. Classification results on E-SAR Oberpfaffenhofen data. (a)~(b) Seven classes initial segment by the proposed scattering mechanism identification after applying FMD and AMD. (c)~(d) The final classification results after iterated clustering corresponding to the initial segmentations shown in (a)~(b).

is 1300×1200 and filtered by a 3×3 boxcar filter. Fig. 8(a) shows the colored image with Pauli matrix components and Fig. 8(b) shows the corresponding optical image. The classification results for the two model-based decompositions are shown in Fig. 9, with the initial classification maps.

The initial seven categories segmentation maps (as shown in Figs. 9(a) and (b)) demonstrate the existence of various complex hybrid scattering mechanisms. In the final classification results, forest and cropland are well classified, the areas with surface and surface hybrid scattering mechanisms are distinguished well for separating airport runways, grassland and bareland. We can recognize the hangars along the runway and the metal reflectors in the airport area. The built-up areas show complex patterns. The building blocks facing to the radar sight directly induces strong double-bounce reflection, and then they are coded with the warmest color.

4. DISCUSSION

The proposed scattering identification scheme aims to solve the problem of more detailed segmentation for pixels whose dominant scattering are not clearly defined. Fig. 2(a) illustrated that only one mixed scattering category is not enough to distinguish the scattering mechanisms contained in complex scenes. The results showed in Fig. 5 and Fig. 6 demonstrated the ability of the proposed scheme to detailed segment the mixed scattering mechanisms. Compared to Lee's [9] and Yang's [21] schemes, the proposed schemes is more direct and the decision criterion is very simple, no predefined threshold is needed.

The proposed scattering mechanism segmentation scheme actually provides an objective tool for analyzing the results obtained by model-based decomposition. We mainly illustrate two typical decomposition algorithms, the FMD and AMD, any other proposed model-based decomposition algorithms [24, 27] can also be analyzed in a similar way. The differences revealed in Fig. 5 and Fig. 6 for FMD and AMD show that the proposed scheme can analyze the result of model-based decomposition effectively, which can help us understanding different decomposition algorithms in a more intuitive way.

We also incorporate our scheme with unsupervised classification, which is a common and classic topic in SAR image processing. The proposed scheme provides good initial segmentations, as shown in Figs. 7(a)~(b) and Figs. 9(a)~(b). The final results showed in Figs. 7(d)~(e) and Figs. 9(c)~(d), demonstrate the initialization is feasible and effective. As we can see, the classification results do not benefit much more from the proposed method, compared to the result in Fig. 7(f). Since the two algorithms both take an iterative Wishart classifier to refine the results, when the number of iterations is large enough, their results will become very similar. The classification strategy we adopted does not make full use of the proposed scattering mechanism identification method, developing a more suitable classification scheme will be a future work.

Our scattering mechanism identification scheme can also be easily extended to the four-component decomposition [28]. Since there are four basic scattering terms, the dimensionality of the normalized scattering vector is four, and it represents a point on standard 3-simplex in \mathbf{R}^4 . The four vertices then represent four pure scattering mechanisms: surface, volume, double-bounce and helix scattering. Considering all the combinations of the four scattering mechanisms, we can totally define 15 categories and their SCCPs in \mathbf{R}^4 . The scattering mechanism identification process is similar to the case of three-component decomposition. However, we should note that, since

the reflection symmetry is approximately hold for the common cases, the magnitude of the helix component may be very low compared with other three terms, how to deal with the pixels with helix-related scattering needs further investigation.

5. CONCLUSION

We have proposed a simple but effective scattering mechanism identification scheme for analyzing the mixed scattering mechanisms obtained by model-based decomposition. By defining the normalized scattering vectors and the SCCPs, we formulated the scattering mechanism identification problem to dividing the 2-simplex in \mathbf{R}^3 by Euclidean distances. Compared to other schemes, the proposed partitioning scheme was intuitively clear and there was no need to worry about the threshold problem. The form of scatter diagram on standard 2-simplex plane also provided a visualization method for analyzing scattering mechanisms of the model-based decomposition. Data analyzing and classification combined with different three-component model-based decomposition on real PolSAR images demonstrated the effectiveness of the proposed scheme.

ACKNOWLEDGMENT

The research was supported in part by the National Key Basic Research and Development Program of China under Contract 2013CB733404, the Chinese National Natural Sciences Foundation grants (NSFC) 61271401 and the research fund of the Key Laboratory of Geoinformatics of National Administration of Surveying, Mapping and Geoinformation, No. K201203.

REFERENCES

1. Ren, S., W. Chang, T. Jin, and Z. Wang, "Automated SAR reference image preparation for navigation," *Progress In Electromagnetics Research*, Vol. 121, 535–555, 2011.
2. Koo, V. C., Y. K. Chan, G. Vetharatnam, M. Y. Chua, C. H. Lim, C.-S. Lim, C. C. Thum, T. S. Lim, Z. Bin Ahmad, K. A. Mahmood, M. H. Bin Shahid, C. Y. Ang, W. Q. Tan, P. N. Tan, K. S. Yee, W. G. Cheaw, H. S. Boey, A. L. Choo, and B. C. Sew, "A new unmanned aerial vehicle synthetic aperture radar for environmental monitoring," *Progress In Electromagnetics Research*, Vol. 122, 245–268, 2012.

3. Mohammadpoor, M., R. S. A. Raja Abdullah, A. Ismail, and A. F. Abas, "A circular synthetic aperture radar for on-the-ground object detection," *Progress In Electromagnetics Research*, Vol. 122, 269–292, 2012.
4. Van Zyl, J. J., "Unsupervised classification of scattering behavior using radar polarimetry data," *IEEE Transactions on Geoscience and Remote Sensing*, Vol. 27, No. 1, 36–45, 1989.
5. Kong, J., S. Yueh, H. Lim, R. Shin, and J. Van Zyl, "Classification of earth terrain using polarimetric synthetic aperture radar images," *Progress In Electromagnetics Research*, Vol. 3, 327–370, 1990.
6. Lee, J.-S., M. R. Grunes, and R. Kwok, "Classification of multi-look polarimetric SAR imagery based on complex wishart distribution," *International Journal of Remote Sensing*, Vol. 15, No. 11, 2299–2311, 1994.
7. Pottier, L., "Dual frequency polarimetric SAR data classification and analysis," *Progress In Electromagnetics Research*, Vol. 31, 247–272, 2001.
8. Ferro-Famil, L., E. Pottier, and J. Lee, "Unsupervised classification of natural scenes from polarimetric interferometric SAR data," *Frontiers of Remote Sensing Information Processing*, Vol. 105, 2003.
9. Lee, J.-S., M. R. Grunes, E. Pottier, and L. Ferro-Famil, "Unsupervised terrain classification preserving polarimetric scattering characteristics," *IEEE Transactions on Geoscience and Remote Sensing*, Vol. 42, No. 4, 722–731, 2004.
10. Cao, F., W. Hong, Y. Wu, and E. Pottier, "An unsupervised segmentation with an adaptive number of clusters using the span/ $h/\alpha/a$ space and the complex wishart clustering for fully polarimetric SAR data analysis," *IEEE Transactions on Geoscience and Remote Sensing*, Vol. 45, No. 11, 3454–3467, 2007.
11. Teng, H. T., H.-T. Ewe, and S. L. Tan, "Multifractal dimension and its geometrical terrain properties for classification of multi-band multi-polarized SAR image," *Progress In Electromagnetics Research*, Vol. 104, 221–237, 2010.
12. Yang, W., Y. Liu, G.-S. Xia, and X. Xu, "Statistical mid-level features for building-up area extraction from full polarimetric SAR imagery," *Progress In Electromagnetics Research*, Vol. 132, 233–254, 2012.
13. Cloude, S. R. and E. Pottier, "An entropy based classification scheme for land applications of polarimetric SAR," *IEEE Transactions on Geoscience and Remote Sensing*, Vol. 35, No. 1,

- 68–78, 1997.
14. Lee, J.-S., M. R. Grunes, T. L. Ainsworth, L.-J. Du, D. L. Schuler, and S. R. Cloude, “Unsupervised classification using polarimetric decomposition and the complex wishart classifier,” *IEEE Transactions on Geoscience and Remote Sensing*, Vol. 37, No. 5, 2249–2258, 1999.
 15. Pottier, E. and J. Lee, “Unsupervised classification scheme of polsar images based on the complex wishart distribution and the $H/A/\alpha$ polarimetric decomposition theorem (polarimetric SAR),” *EUSAR 2000*, 265–268, 2000.
 16. Song, H., W. Yang, X. Xu, and M. Liao, “Data-driven polinsar unsupervised classification based on adaptive model-based decomposition and Shannon entropy characterization,” *Progress In Electromagnetics Research B*, Vol. 49, 215–234, 2013.
 17. Zakeri, B. G., A. Ghorbani, and H. R. Amindavar, “A new method to extract the polarimetric parameters in imaging radars,” *Progress In Electromagnetics Research*, Vol. 87, 167–182, 2008.
 18. Du, Y., W.-Z. Yan, J.-C. Shi, Z. Li, and E.-X. Chen, “Electromagnetic scattering from a corn canopy at L and C bands,” *Progress In Electromagnetics Research*, Vol. 114, 33–49, 2011.
 19. Cloude, S. R. and E. Pottier, “A review of target decomposition theorems in radar polarimetry,” *IEEE Transactions on Geoscience and Remote Sensing*, Vol. 34, No. 2, 498–518, 1996.
 20. Freeman, A. and S. L. Durden, “A three-component scattering model for polarimetric SAR data,” *IEEE Transactions on Geoscience and Remote Sensing*, Vol. 36, No. 3, 963–973, 1998.
 21. Yang, W., T.-Y. Zou, H. Sun, and X. Xu, “Improved unsupervised classification based on Freeman-Durden polarimetric decomposition,” *2008 7th European Conference on Synthetic Aperture Radar (EUSAR)*, 1–4, 2008.
 22. Lee, J.-S. and E. Pottier, *Polarimetric Radar Imaging: From Basics to Applications*, 1st Edition, 422, CRC Press, 2009.
 23. Alvarez-Perez, J. L., “Coherence, polarization, and statistical independence in Cloude-Pottier’s radar polarimetry,” *IEEE Transactions on Geoscience and Remote Sensing*, Vol. 49, No. 1, 426–441, 2011.
 24. An, W., Y. Cui, and J. Yang, “Three-component model-based decomposition for polarimetric SAR data,” *IEEE Transactions on Geoscience and Remote Sensing*, Vol. 48, No. 6, 2732–2739, 2010.

25. Van Zyl, J. J., M. Arii, and Y. Kim, "Model-based decomposition of polarimetric SAR covariance matrices constrained for nonnegative eigenvalues," *IEEE Transactions on Geoscience and Remote Sensing*, Vol. 49, No. 9, 3452–3459, 2011.
26. Arii, M., J. J. van Zyl, and Y. Kim, "Adaptive model-based decomposition of polarimetric SAR covariance matrices," *IEEE Transactions on Geoscience and Remote Sensing*, Vol. 49, No. 3, 1104–1113, 2011.
27. Cui, Y., Y. Yamaguchi, J. Yang, and H. Kobayashi, "On exact model-based scattering decomposition of polarimetric SAR data," *2012 IEEE International Symposium on Antennas and Propagation (ISAP)*, 106–109, 2012.
28. Yamaguchi, Y., T. Moriyama, M. Ishido, and H. Yamada, "Four-component scattering model for polarimetric SAR image decomposition," *IEEE Transactions on Geoscience and Remote Sensing*, Vol. 43, No. 8, 1699–1706, 2005.
29. Yamaguchi, Y., A. Sato, W.-M. Boerner, R. Sato, and H. Yamada, "Four-component scattering power decomposition with rotation of coherency matrix," *IEEE Transactions on Geoscience and Remote Sensing*, Vol. 49, No. 6, 2251–2258, 2011.
30. Sato, A., Y. Yamaguchi, G. Singh, and S.-E. Park, "Four-component scattering power decomposition with extended volume scattering model," *IEEE Geoscience and Remote Sensing Letters*, Vol. 9, No. 2, 166–170, 2012.
31. Zhang, J. J., P. Wang, L. Chen, Y. Li, Q. Yin, and W. Hong, "Seven-category model-based segmentation for polarimetric SAR data," *PolInSAR'13*, ESA, Frascati, Italy, Jan. 28–Feb. 1, 2013.
32. Arii, M., J. J. van Zyl, and Y. Kim, "A general characterization for polarimetric scattering from vegetation canopies," *IEEE Transactions on Geoscience and Remote Sensing*, Vol. 48, No. 9, 3349–3357, 2010.